IAC-25-C1

HIGH-RESOLUTION IMAGING IN VLEO: PRELIMINARY MISSION ANALYSIS AND GNC DESIGN FOR THE HORUS MISSION

Andrea Jimmy Pacursa[a*], Manuel Cappuccio[a], Matteo Braga[a], Davide Bellini[a], Matteo Giovanni Juvara[a], Matteo David Dowell[a], Francesco Cataffo[a], Lorenzo Cesarini[a], Giacomo Biraghi[a], Beatrice Beretta[a], Michèle Roberta Lavagna[b]

[a] *MSc in Space Engineering, Department of Aerospace Science and Technology, Politecnico di Milano, Via La Masa 34, 20156 Milano, Italy*

[b] *Full Professor, Department of Aerospace Science and Technology, Politecnico di Milano, Via La Masa 34, 20156 Milano, Italy*

[*] *Corresponding author, andreajimmy.pacursa@mail.polimi.it*

Abstract

The Very Low Earth Orbit (VLEO) environment is rapidly gaining attention for Earth Observation (EO) missions due to its numerous advantages. Satellites operating at this altitude can achieve cost-effective high-resolution imaging, improved revisit time, and exploit reduced communication power and a cleaner orbital environment with less space debris. Within this framework, the High-resolution Orbiting Reconnaissance and Universal Surveillance (HORUS) mission feasibility study has been carried out over four months at Politecnico di Milano.

HORUS is an Earth Observation mission aimed to acquire high-resolution images with minimal latency, while operating in the VLEO region. The primary drivers of the mission are an high spatial resolution, set to be less than 1 m, and a revisit time lower than one day. To meet these requirements, the satellite architecture must be tailored accordingly, with a particular attention to the Mission Analysis (MA) design.

VLEO operations pose significant challenges due to high atmospheric drag and zonal harmonic effects, complicating station-keeping. To address this, the orbital parameters are optimized to minimize drag compensation costs and Right Ascension of the Ascending Node (RAAN) drift due to $J2$ perturbations while keeping launch costs limited. The mission features a scalable formation flight concept, where drones in the same orbital plane provide regional coverage, with the possibility to add multiple planes to improve revisit time. This modular approach enhances operational flexibility, allowing customers to define their coverage area and imaging schedule, from cities ($\approx 200\ km^2$) to medium-sized countries ($\approx 40\,000\ km^2$). High-resolution imaging of the same target requires robust orbit control and adaptive guidance strategies. Continuous assessments of trajectory deviations enable autonomous correction maneuvers, keeping the spacecraft within a defined virtual slot and ensuring precise synchronization with targets. Longitude errors, which impact imaging accuracy, are actively constrained through a Directional Adaptive Guidance (DAG) strategy, dynamically adjusting the spacecraft's motion to maintain the correct positioning. This approach optimizes station-keeping operations, reducing propellant consumption and ensuring persistent coverage.

The paper will discuss the design trade-offs, operational strategies, and optimization techniques employed by HORUS, highlighting the integration of scalable mission architectures, formation flight flexibility, and autonomous guidance solutions. Furthermore, the achievable performances are thoroughly analyzed, highlighting the opportunities this flexible mission design can offer for future EO missions operating at these very low altitudes.

Acronyms

ADCS Attitude Determination and Control System

BC Ballistic Coefficient

DAG Directional Adaptive Guidance

ECSS European Cooperation for Space Standardization
EO Earth Observation
EPS Electrical Power System
ESA European Space Agency

FoV Field of View

GNC Guidance, Navigation and Control
GOCE Gravity Field and Steady-State Ocean Circulation Explorer

HEET Hall-Effect Electric Thruster
HORUS High-resolution Orbiting Reconnaissance and Universal Surveillance

LEO Low Earth Orbit

MA Mission Analysis

RAAN Right Ascension of the Ascending Node
RCN Radial-Conormal-Normal
ROE Relative Orbital Elements

SSO Sun Synchronous Orbit
SW Swath Width

TCS Thermal Control System
TRL Technology Readiness Level
TTMTC Telemetry, Tracking, and Telecommand

UTC Coordinated Universal Time

VLEO Very Low Earth Orbit

1 Introduction

Operating a satellite in VLEO is not an easy task, but such a unique environment introduces some important advantages in mission profiles [1]. The relative vicinity to Earth's surface allows to acquire high resolution images without the need for extreme (and costly) imaging solutions; the reduced orbital period, if combined with a repeating ground track strategy, makes it possible to have periodic and frequent passages over the same coordinates, either for target imaging updates or communication with a ground station. On the other hand, the harsh environment poses critical challenges during the preliminary design phases: Earth's harmonics (primarily J_2) and atmospheric drag significantly affect station keeping and mission lifetime, and must therefore be accurately modeled and carefully accounted for in mission design and Guidance, Navigation and Control (GNC) strategy.

HORUS is a Earth Observation mission, whose ultimate goal is to demonstrate and achieve a balance between the benefits and drawbacks of the environment it will operate within: conducting high-resolution imaging, exploiting the surface proximity and the frequent passages over a selected target, while managing the strong decay and turbulence imposed by its surroundings. When outlining the mission, the critical aspects regarding the Mission Analysis and GNC design were thoroughly explored and different solutions were introduced and tested.

This paper aims to highlight the key foundations of the concurrent engineering design process, as well as to present some intermediate steps and the final Mission Analysis and GNC solutions implemented in order to tackle the challenges posed by the VLEO environment, within the context of an iterative design of all the other subsystems. This work is organized as follows: **Section 2** highlights a series of precedents from which the design process has taken inspiration and wisdom; in **Section 3** the Mission Analysis requirements and strategies are detailed, with a glance on the payload, telecommunication and power supply choices together with the mission's defining feature of target revisit. **Section 4** outlines the GNC strategy, starting from a proper environmental study and culminating in the definitions of virtual slot and Directional Adaptive Guidance. Finally, **Sections 5** and **6** provide a concise yet accurate analysis of the simulation outputs, underlining the achievements as well as the limitations of the mission concept.

2 State of the Art

Not many missions have selected VLEO as their operative field, due to the technical challenges that this harsh environment arises. However, especially in recent years, various concepts have been developed and some groundbreaking VLEO missions have seen the light.

ESA's Gravity Field and Steady-State Ocean Circulation Explorer (GOCE) was probably the most renowned of them all [2]. Launched in 2009, it demonstrated the feasibility of operating in VLEO environment, as it orbited at 255 km of altitude. At the core of GOCE's GNC strategy there was a drag-free control system with xenon ion thrusters and ultra-sensitive accelerometers, that allowed the spacecraft to maintain precise real-time control over its orbit and attitude [3].

Another relevant example of a VLEO mission is the QARMAN 3U CubeSat [4], designed to validate semi-controlled differential drag maneuvers through surface area modulation for both orbit control and de-orbiting. The passive AeroSDS system ensured attitude stability in VLEO and during re-entry, thereby demonstrating that aerodynamic surfaces can provide efficient and resource-conservative GNC solutions for small satellites.

Finally, Planet Labs' SuperDove platform and their Flock Imaging Constellation must be mentioned as it represents a pioneer mission for Earth-imaging constellations in VLEO [5]. SuperDove proved the advantages of low-altitude constellations for imaging and highlighted the main drawbacks and problems faced by small satellites at these altitudes.

Previous studies of constellation orbits have been consulted to better understand their effects on mission performances during mission analysis design [6]. In particular, Walker and Street-of-Coverage constellations are constellation designs that can achieve continuous global coverage while balancing other factors such as the need for collision avoidance and station-keeping maneuvers. Their configuration is defined by characteristic parameters, which can be adjusted by designers to trade off between coverage quality, operational resilience, and life-cycle management, in order to optimize specific mission performances.

Regarding the station-keeping, studies have shown how continuous low-thrust propulsion is a very effective solution for station-keeping and insertion maneuvers at very low altitudes [7] when paired with a precise Attitude Determination and Control System (ADCS). Furthermore, the use of a Relative Orbital Elements (ROE) model for formation flying acquisition and maintenance has been proven to optimize fuel efficiency and tracking accuracy [8].

Directional Adaptive Guidance could be a suitable choice due to its effectiveness for low-thrust missions. DAG has been shown to enable near-optimal trajectory control with minimal post-optimization tuning requirements, even in the presence of continuous perturbations [9]. By adaptively steering thrust direction to target specific orbital elements, these guidance laws can efficiently achieve mission goals while reducing propellant use and transfer time [10]. This flexibility is extremely valuable in environments where strong perturbations and system uncertainties demand continuous adjustment of the control strategy.

3 Mission Analysis

The first step of HORUS Mission Analysis involves the identification of the nominal orbit for operations, in compliance with the following high-level mission requirements:

- To acquire high-resolution images, with spatial resolution below 1 m.
- To monitor a fixed target on the surface with a time resolution within 1 day.
- To downlink within 1 hour from acquisition.
- To operate in VLEO for Technology Readiness Level (TRL) demonstration.
- To guarantee flexibility in terms of target coverage.

3.1 Orbital Parameters

To guarantee the passage over a specific target at least once a day, the design of an orbit with repeating ground track is desirable. Imposing 16 revolutions of the satellite every day, the semi-major axis and therefore the mean operative altitude are obtained within the VLEO range.

Regarding the eccentricity of the nominal orbit, under the hypothesis of continuous thrusting and adopting an exponential atmospheric density model, the drag compensation cost becomes a driver: regardless the assumptions on drag coefficient and area-to-mass ratio, simulations have shown that the optimal orbit would be a circular one, as depicted in Fig. 1.

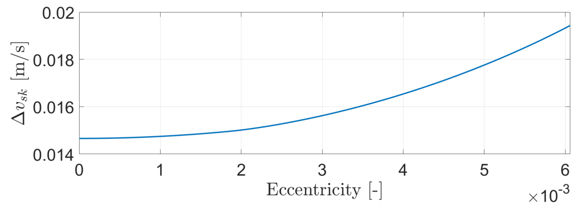

Figure 1: ΔV per orbit for drag compensation ($C_d = 2$ and $\frac{A_{\text{cross}}}{\text{mass}} = 0.001\ \frac{m^2}{kg}$)

With regard to the other relevant orbital parameters, it is clear that they will depend on the application, on the operational epoch, and on the specified target on ground. Another major aspect to assess is the downlink strategy to deliver the images on ground: if no perturbations are considered, given the semi-major axis and the eccentricity, a properly inclined orbit which passes over two points on the surface, taking into account Earth rotation, always exists, as shown in Fig. 2.

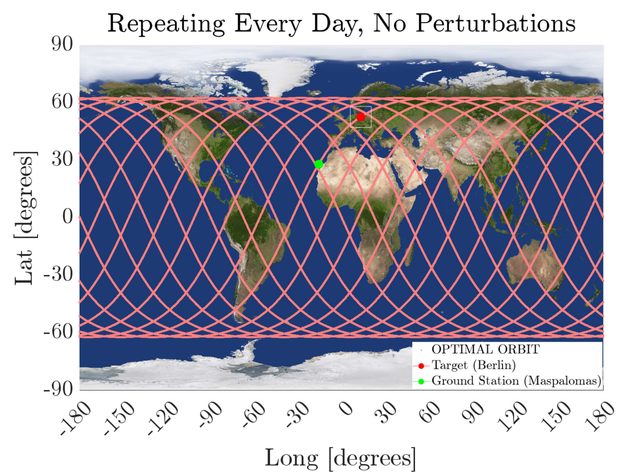

Figure 2: Representative example of a retrograde orbit passing over target, then ground station

This would allow to tailor the orbital plane depending on the application and on the selected ground station, and this works with atmospheric drag perturbation as well, if properly compensated. However, once the zonal harmonics effects are factored in, this ideal scenario shows its weaknesses. In a preliminary analysis, the orbital plane drift due to the $J2$ effect is definitely the major issue, as graphically shown in Fig. 3.

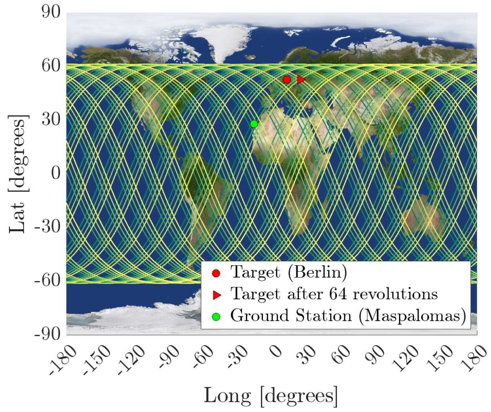

Figure 3: $J2$ effect on the ground track over 64 revolutions (4 days)

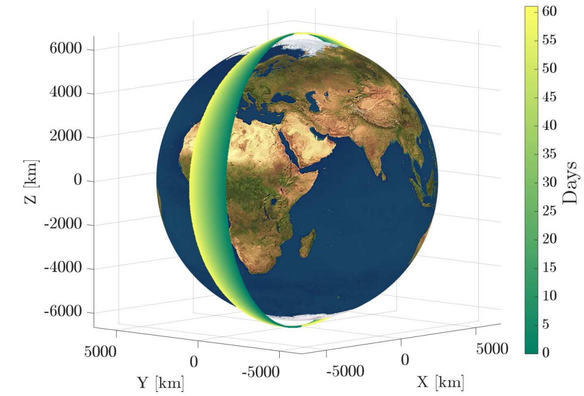

Figure 4: J2 effect on a 88° inclined orbit over two months

Table 1: Observation window in days for different latitudes for a single satellite operating in SSO

Latitude $[deg]$	**Days**
0	8.35
15	8.64
30	9.34
45	11.80
60	16.69
75	32.25

Since the secular RAAN drift is linearly dependent with the cosine of the inclination, the candidate solutions were reduced to orbital planes with an inclination between 80° and 100°. In Fig. 4, the effect on a Sun Synchronous Orbit (SSO) is reported, and this is better quantified in Table 1: taking a bunch of target latitudes to observe, the visibility windows are computed considering a maximum slew angle of the satellite of 25°.

Such small observation windows are not acceptable, so the drift compensation has been evaluated, leading to the unaffordable cost of $40.70\,m/s$ per day.

At this point, there are two possible architectures: a constellation of drones placed in equally spaced inclined orbits, ensuring continuous observability over the target, or a single drone in a polar orbit to cancel the RAAN drift. After some design iterations, ground station availability, downlink capabilities, cost and complexity assessments, the circular and polar orbit architecture has been chosen, with a nominal altitude of $262.75, km$ ensuring repeating ground track, and nominal RAAN which will be determined depending on the target longitude and reference epoch specified by the customer. Furthermore, this architecture keeps the door open to several coverage and revisit-time scalable strategies, totally tailored on the application.

3.2 Orbital Insertion

The initial orbital insertion maneuver must be designed to be efficiently performed by an electric thruster, chosen for this mission. The initial assumptions are that the launcher inserts the spacecraft on an orbit with an inclination of 90°, a RAAN deriving from the target and epoch selected and an altitude of 500 km, which is a standard LEO altitude. After performing commissioning, the spacecraft performs an orbital maneuver to reach the nominal orbit.

The maneuver is performed through continuous thrusting assuming to use maximum thrust during the sunlight period of the orbit and by completely switching off the propulsive system when in eclipse, which is approximately 35% of the orbit. The solar disturbances are assumed at a minimum, as the air drag and other related disturbances favor this maneuver. The computed ΔV cost of this maneuver is approximately 130 m/s, including all necessary compensation of RAAN and inclination drifting.

Initially the satellite shall rotate by 180° before firing, using on-board actuators, as the thruster shall fire in the opposite direction of the satellite velocity to slow down the spacecraft. The thruster will start firing once the spacecraft has finished performing its slew.

3.3 Disposal Strategy

Although this altitude range is not highly congested, de-orbiting remains a fundamental aspect of mission design. Satellites are required by regulation to re-enter the atmosphere or to be relocated to graveyard orbits within 5 years after mission completion [11], making orbital decay a critical factor to consider.

The rate of orbital decay is influenced by several factors, including initial orbit features and the Ballistic Coefficient (BC). Satellites with a lower BC typically decay more rapidly due to higher air drag effects. Studies indicate that small satellites at altitudes below 400 km can decay naturally in under 5 years [12]. The high atmospheric drag at these altitudes provides an opportunity to implement simple and cost-saving disposal solutions leveraging natural atmospheric drag in VLEO.

3.4 Payload Selection and Imaging

After some iterations the main payload was chosen among a few candidates for its high performances and pertinence with the desired specifics. The selected on-board camera is Satlantis' iSIM-90 [13] in its dual-channel configuration, which can fulfill the spatial resolution requirement as well as survive the VLEO environment.

Table 2: iSIM-90 (dual channel) technical specifics

Focal Length $[mm]$	1667
Max Alt. $[km]$ $(GSD \leq 1\,m)$	303
Mass $[kg]$	< 6
Dimensions $[mm]$	$308 \times 216 \times 115$
Power $[W]$	30.5
Field of View (FoV) $[deg]$	1.49 to 2.98
Swath $[km]$ **(@ Max Alt.)**	7.88 to 15.76
Bands	PAN, VNIR (< 8)
Storage $[GB]$	500
Thermal Control	Active

3.5 Ground Stations and Downlink Capabilities

Ensuring a worldwide and swift coverage was one of the pillars of the HORUS mission design. The spacecraft is provided with a set of patch antennas that convey and receive the signals over the bottom half hemisphere of the main body. This wide FoV guarantees, together with a high-performance on-board amplifier, the minimization of the time needed to up and downlink the information.

Another fundamental aspect of the coverage analysis was the availability of a wide spread ground station network able to receive and transmit from and to the spacecraft. The final selection of 25 ground stations, drawn from ESA's ESTRACK network [14] as well as commercial providers such as LeafSpace [15] and the Swedish Space Corporation [16], was driven by the fundamental requirement of ensuring that the spacecraft establishes contact with at least one station within one hour of image acquisition. This condition was likewise extended to the multi-satellite configuration. Due to design constraints, a limit of 20 aligned drones has been identified to guarantee complete retrieval of all the data gathered during the observations.

Fig. 5 shows the final solution and the ground station network (with yellow dots representing ESTRACK stations and cyan dots signaling commercial ones), in which the colors represent the latency time between acquisition and downlink of the pictures. As shown, every point on the Earth's surface is serviced by HORUS with a latency lower than 60 minutes, as demanded by the mission requirements.

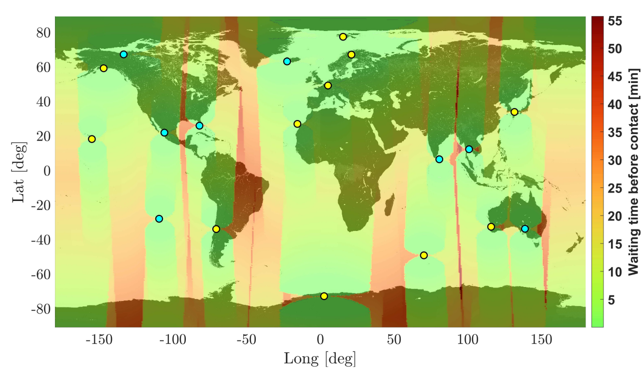

Figure 5: Global coverage and performance analysis

3.6 Coverage Analysis

This section will assess to what extent a scalable architecture design is effective and flexible with respect to various coverage needs. Starting from the optical payload specifications presented in Section 3.4, and the nominal altitude $h = 262.75\,km$, the performances in terms of resolution and across-track width for a single drone nadir pointing equipped with two optical payloads are:

$$SW = 2\ h\ atan\,(FoV) = 13.21\ km \tag{1}$$

$$GSD = \frac{p\ h}{f} = 0.87\ m \tag{2}$$

with an along-track Swath Width (SW) of:

$$SW_{along} = 2\ h\ atan\left(\frac{FoV}{2}\right) = 6.60\ km \tag{3}$$

It is important to remark that a margin of about $0.1°$ has been taken into account, leading to $\approx 97\%$ of the swath effectively covered during operations. This is a useful margin from the redundancy point of view while considering the formation flying.

At this point, the target coverage flexibility is evaluated: a possible architecture solution which aims to enlarge the overall footprint on ground while exploiting the same orbital plane to minimize launch costs is to adopt a formation flying made of a row of drones lined up.

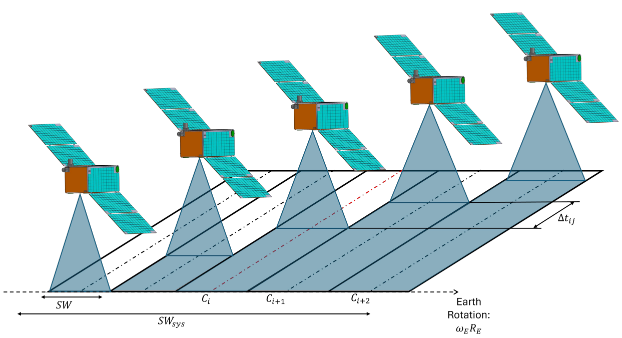

Figure 6: Formation flying concept, leveraging on Earth rotation

The system of drones depicted in Fig. 6 is capable of reconstructing a bigger image, composed by the different stripes associated to the sequential passages of each satellite, exploiting the Earth rotation. Thus, considering square coverage (i.e. equal across-track and along-track image dimensions), the total covered surface by the formation is:

$$A_{cov,max} = SW_{sys}\ n_{drones}\ SW \tag{4}$$

Another strategy to increase the coverage performance is to impose a non-null roll angle while acquiring images. Knowing that the maximum distance to ensure less than $1\,m$ resolution is $303\,km$ from ground (Table 2), and exploiting some basic trigonometric formulas, the maximum roll slew angle achievable during the imaging mode is $28.44°$. In this way, the across-track Swath Width is increased to $SW = 16.74\,km$ for a single drone. The drawback consists in a reduction of the spatial resolution performance, which keeping some margin on the maximum roll slew angle amounts at $0.99\,m$.

At this point, it is important to assess the relative shift in true anomaly between different drones of the same formation. The idea is that, taking the tracks on ground related to the respective boresights of each drone, they can be converted to information on the difference in longitude $\Delta\lambda$ from one track to the adjacent ones, due to Earth rotation. Denoting C_i the center of the $i-th$ stripe, as in Fig. 6, this is computed, for half of the symmetric formation, depending on the number of drones employed.

$$\begin{cases} C_i = (2i-1)\frac{SW}{2}, & \text{if } n_{drones} \text{ even} \\ C_i = 2i\frac{SW}{2}, & \text{if } n_{drones} \text{ odd} \end{cases} \tag{5}$$

The peculiarity of a polar orbit is that its ground track is a perfectly straight line in the longitude-latitude plane. Furthermore, the angle α_{tilt} between the ground track and the local North-South axis is constant. Given any time interval dt and the associated true anomaly $d\theta$ spanned in the associated circular orbit arc, the following relation holds:

$$\alpha_{tilt} = \arctan\left(\frac{\omega_E\ dt}{d\theta}\right) = 3.58° \tag{6}$$

where ω_E is the Earth angular velocity. Once the ground coverage stripes centers are available, the relative distances $C_{shift,ij}$ with the adjacent ones are exploited to compute the distance on the parallel related to the target latitude φ_T:

$$\Delta\lambda_{km,ij} = \frac{C_{shift,ij}}{\cos\left(\alpha_{tilt}\right)} \tag{7}$$

$$\Delta\lambda_{ij} = \Delta\lambda_{km,ij}\ \frac{360°}{2\pi R_E \cos\left(\varphi_T\right)} \tag{8}$$

Finally, referring to Fig. 6, the time delay between two consecutive drones and the corresponding true anomaly shift in the common orbital plane are easily recovered.

$$\Delta t_{ij} = \frac{\Delta\lambda_{ij}}{\omega_E} \qquad \Delta\theta_{ij} = \frac{\Delta t_{ij}\ 360°}{T_{orb}} \tag{9}$$

3.7 Revisit Time

Up to now, the circular and polar orbit selected ensures that a repeating ground track is obtained, but every drone passes above the target area just once a day. Further considerations and solutions are needed to improve the revisit time performances and ensure scalability of the architecture.

Thinking about the single drone architecture, a first solution, which exploits the same orbital plane to minimize launch and insertion costs, is to put a second drone that takes an image 12 h after. In fact, as the target rotates with the Earth, it crosses the orbital plane twice a day.

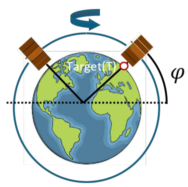

Figure 7: Doubling the revisit time

From Fig. 7 it is clear that the shift in true anomaly depends on the target latitude:

$$\theta_2 = \theta_1 + 180^\circ - 2\varphi_T \tag{10}$$

Similarly, the epoch at which the imaging operations are performed is strictly linked with the RAAN and the target longitude.

$$\Omega = \lambda_T + 360^\circ \left(\frac{Date_{j2000} - Spring_{j2000}}{365.25\ days} \right) \tag{11}$$

The revisit time performance can be further improved, leveraging on the circular and polar nominal orbit properties: multiple orbital planes can be exploited and, depending on schedule requirements and time delays between consecutive imaging modes, the shift in RAAN can be determined.

$$\Delta\Omega = \Delta t_h\ 15^\circ/h \tag{12}$$

In each orbital plane, the drones shall be precisely synchronized to ensure the passage above the target at a certain epoch, considering the Earth rotation. Selecting a reference epoch, the time of flight until the imaging epoch and the initial condition in terms of true anomaly are recovered:

$$ToF = \frac{\Delta t_h\ 2\pi}{24\ \omega_E} \qquad \theta_0 = -\sqrt{\frac{\mu}{a^3}}\ ToF \tag{13}$$

where Δt_h is the time difference in hours between the reference epoch and the desired imaging epoch, and θ_0 is the starting true anomaly considering for simplicity, since the nominal orbit is circular, the perigee above the target.

3.8 EPS Strategy

The design of the Electrical Power System (EPS) is subject to several critical constraints arising from the peculiar orbital environment. Particularly, due to the spacecraft operating in VLEO at a non-sun-synchronous altitude, strong variations in illumination and thermal conditions are experienced over its lifetime. These variations are highly dependent on the choice of the RAAN, in turn determined by target selection. For instance, with a RAAN of $\Omega = 90^o$, two extreme scenarios emerge (Fig. 8): near the solstices, eclipses reach durations of up to 37 minutes, representing a severe constraint for both solar array and battery design; conversely, near the equinoxes, eclipse-free periods of up to 30 consecutive days occur, imposing critical challenges for the Thermal Control System (TCS).

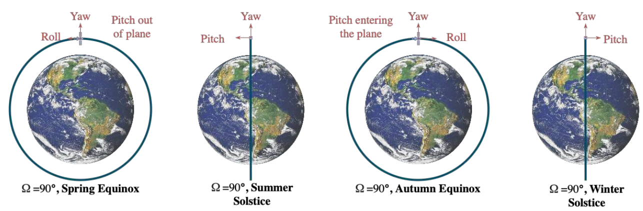

Figure 8: Orbit from Sun point of view at different times of the year ($\Omega = 90^o$)

In addition, the requirement to minimize the spacecraft's cross-sectional area for drag reduction leads to a non-standard attitude control approach for Sun pointing, hereafter referred to as "planar Sun pointing." In this mode, the Sun aspect angle is maximized solely through maneuvers about the roll axis. With the solar panel configuration as depicted in Fig. 9, this strategy proves effective around the equinoxes, where high pointing efficiency can be achieved; however, near the solstices the reduced controllability along other axes prevents optimal Sun tracking, resulting in degraded performance. The control, for the case study with $\Omega = 90^o$, has a very marked oscillatory behavior, as depicted in Fig. 10. Hence, filtering was introduced to achieve a smooth slew-angle profile of approximately 1^o per day over the year.

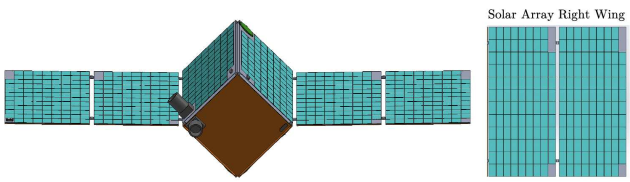

Figure 9: Solar panels configuration

EPS sizing is therefore performed in the worst-case scenario, i.e. at the solstices, where both solar array power generation and battery capacity face their most stringent demands.

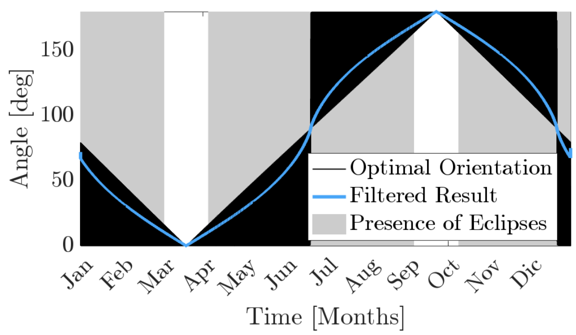

Figure 10: Solar panels optimal orientation (measured about the roll axis, starting from the pitch axis)

Furthermore, the adoption of an electric thruster has an additional impact on the overall power budget. In the end, the thrusting maneuvers are performed during the sunlight phase of each orbit, reducing the potential burden on the batteries. Fig. 11 reports the average power produced and requested by the solar arrays per orbit over the time span of one year.

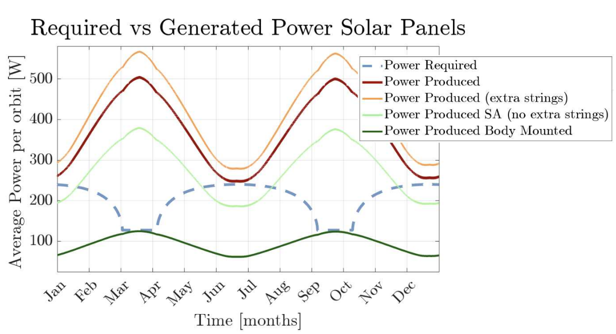

Figure 11: Average power produced vs power required during one year, with $\Omega = 90^o$

Two distinct operating conditions are highlighted in the plot. At the solstices, when eclipse duration peaks the power demand reaches its maximum, driven by battery recharging requirements. Furthermore, Sun pointing efficiency is strongly reduced due to the aforementioned limitations. Hence, this case governs the EPS sizing. At the equinoxes, in contrast, pointing efficiency improves significantly and power requests from the batteries drops, due to the shorter-to-absent eclipses. This results in potential power surpluses. Since excess power would impose unacceptable dissipation requirements on the TCS, a mitigation strategy is implemented by rotating the spacecraft away from the peak power production point to intentionally reduce the solar input.

4 Guidance and Control Strategy

Effective Guidance and Control strategies are essential for precise orbit maintenance and optimal imaging performance. This section introduces the adopted strategy, based on DAG, designed to ensure robust control performance in the challenging VLEO environment.

4.1 Drag Effects and BC Analysis

In VLEO environments, spacecraft dynamics are predominantly influenced by atmospheric drag, characterized through the Ballistic Coefficient. The BC models the relationship between inertial and aerodynamic forces acting on the satellite, and is defined as:

$$BC = \frac{m}{A_{cross}\, C_D} \tag{14}$$

where m is the spacecraft mass, A_{cross} is the cross-sectional area perpendicular to the velocity vector, and C_D is the drag coefficient.

Higher values of BC indicate greater inertia relative to aerodynamic forces, resulting in reduced sensitivity to drag. Conversely, lower BC values imply a stronger influence of atmospheric drag on the orbital evolution. Since mass, geometry, and aerodynamic properties evolve during the design process, the BC must be assessed iteratively. This requires accounting for variations in configuration and attitude, as well as applying design margins to ensure robustness in orbit insertion and station-keeping performance.

4.2 Station Keeping Strategy

The selected operational altitude for HORUS lies below 300 km, where residual atmospheric density produces non-negligible drag forces. In the absence of compensation, this perturbation causes continuous orbital decay, reducing both semi-major axis and eccentricity. A continuous station-keeping strategy is therefore mandatory.

The aerodynamic acceleration is modeled by:

$$\mathbf{a}_{\text{drag}} = -\frac{1}{2}\frac{A_{\text{cross}}C_D}{m}\rho(h,t)v_{\text{rel}}^2\frac{\mathbf{v}_{\text{rel}}}{|\mathbf{v}_{\text{rel}}|} \tag{15}$$

where $\rho(h,t)$ is the atmospheric density and $\mathbf{v}_{\text{rel}}$ is the velocity relative to the rotating atmosphere.

Since air density varies with altitude, latitude, and solar activity, it was modeled using both the *Jacchia-Bowman* and *NRLMSISE-00* atmospheric models [17], [18]. As expected, the two models provide similar results; therefore, the latter was selected due to its shorter execution time. A preliminary analysis at nominal altitude was conducted to compute the cumulative Δv due to drag.

The simulations confirmed a strong dependence of the required daily Δv on solar activity and the selected ballistic coefficient, reinforcing the importance of adopting conservative design margins for the propulsion system and attitude configuration.

4.3 Virtual Slot Concept

To manage orbital deviations due to drag and ensure imaging accuracy, HORUS relays on a virtual slot. This slot defines a tridimensional region within which deviations from the nominal trajectory do not deteriorate the imaging performances. The spacecraft state is continuously compared against the slot boundaries; whenever a violation occurs, corrective maneuvers are triggered.

Assuming a polar, nearly circular orbit, drag and J_2 effects are confined to the orbital plane. However, a small cross-track tolerance is still included to monitor anomalies. The slot dimensions are derived from a maximum allowable pointing error $\Delta\lambda_{err}$, converted into a true anomaly shift:

$$\begin{cases} \Delta t_{err} = \frac{\Delta\lambda_{err}}{\omega_E} \\ \Delta\theta_{err} = \frac{2\pi\Delta t_{err}}{T_{orb}} \end{cases} \tag{16}$$

The along-track dimension is then defined as:

$$\text{Slot}_{\text{along-track}} = 2a\Delta\theta_{err} \tag{17}$$

To evaluate the radial tolerance, the same angular error is mapped into a variation in orbital period and thus in semi-major axis:

$$a_{new} = \left(\mu_E\left(\frac{\Delta\lambda - \Delta\lambda_{err}}{2\pi\omega_E}\right)^2\right)^{1/3} \tag{18}$$

$$\text{Slot}_{\text{nadir-zenith}} = 2(a - a_{new}) \tag{19}$$

This framework enables threshold-based corrective logic while maintaining phase and altitude consistency with the ground track. The most stringent constraints are associated with equatorial imaging targets, where the slot becomes minimal in both dimensions.

4.4 Directional Adaptive Guidance

Atmospheric drag in VLEO continuously perturbs the orbital elements, leading to the progressive degradation of the repeating ground track. To counteract this effect, HORUS implements a Directional Adaptive Guidance scheme, building upon the methodologies described in [9, 10], in which corrective thrusting is applied only when deviations from the nominal orbit exceed predefined thresholds.

The nominal reference is propagated without disturbances, while the actual orbit includes drag-induced decay. Once the spacecraft exits its allowable region, thrust is engaged and maintained until the deviation is corrected. The thrust directions are calculated in the Radial-Conormal-Normal (RCN) frame using two angles, α and β, optimized to maximize the rate of change of each orbital element as a function of the true anomaly θ.

For each orbital element, an optimal pair of thrusting angles (α, β) is defined based on analytical considerations [9]. For instance, correcting the semi-major axis requires thrusting primarily in the radial direction, while eccentricity control demands a direction that varies with the true anomaly within the orbital plane. These angles are analytically defined for all six Keplerian elements. The resulting thrust unit vector is:

$$\mathbf{f}_{oe} = \begin{bmatrix} f_R \\ f_S \\ f_W \end{bmatrix} = \begin{bmatrix} \cos(\beta)\sin(\alpha) \\ \cos(\beta)\cos(\alpha) \\ \sin(\beta) \end{bmatrix} \tag{20}$$

An adaptive ratio is defined for each orbital element to reflect its relative deviation from the target and scale its influence in the thrust computation:

$$R_{oe} = \frac{oe_T - oe}{oe_T - oe_0} \tag{21}$$

where oe is the current value, oe_T the target, and oe_0 the value at the start of thrusting maneuver. The total thrust direction is obtained by a weighted sum:

$$\mathbf{f}_T = \sum_{oe} R_{oe} W_{oe} \mathbf{f}_{oe} \tag{22}$$

where W_{oe} is the element weight, favoring control of the semi-major axis and eccentricity. Thrust is assumed to be applied at fixed level, always aligned with $\mathbf{f}_T$, and deactivated once the satellite reenters the allowable region.

Accurate phasing plays a key role in ensuring the required coverage of the target area and to maintain proper formation flight among the satellites. To this end, the target semi-major axis is adaptively updated at each time step. The correction is derived from the argument of latitude difference δu between the actual orbit and the reference, according to [19]:

$$a_{\text{target,new}} = \left(K_u \delta u + \sqrt{\frac{1}{a_{\text{target}}}} \right)^{-\frac{2}{3}} \tag{23}$$

Here, K_u is a tunable gain that regulates the influence of phase mismatch on the orbital period. When δu approaches zero, the modified target value converges to the nominal semi-major axis. This formulation ensures synchronized ground track alignment while minimizing excessive control effort.

The updated strategy focuses on controlling the semi-major axis and eccentricity, assigning zero weights to inclination and RAAN due to the polar nature of the orbit. These elements are still monitored, and in case of unexpected deviations, the system can reorient the thruster and apply out-of-plane corrections. The argument of perigee is excluded due to the near-circularity of the operational orbit.

The implemented control logic constrains the Virtual Slot bounds in the nadir–zenith direction to ensure thrust activation at each orbital pass, compensating for density variations driven by solar activity and RAAN evolution. The thrust level is modulated accordingly to maintain regular correction intervals while preserving imaging performance. Maneuvers are applied over short durations once per orbit, with the direction defined through the DAG framework, providing robust orbital maintenance throughout the mission timeline.

5 Results

5.1 Coverage Performances

Considering the preliminary formulation presented in Section 3.6, the coverage performances depend on the number of drones and on the payload specifications. While the field of view and the maximum swath width are given from the payload datasheet, the maximum number of drones depends on several factors. Within the design iterations process, a limit on the along-track image acquisition came out from the Telemetry, Tracking, and Telecommand (TTMTC) subsystem sizing: a maximum of 20 consecutive images can be performed, to ensure that the high level objective of being capable to download the acquired data within 1 h is met.

For this reason, square images are allowed for formation flights up to 10 drones, while for more numerous formations this limit is considered in the computation of the maximum coverage area and Eq. (4) is rewritten as:

$$A_{cov,max} = SW_{sys}\ 20\ SW_{along} \tag{24}$$

After this considerations, considering the formation flying in the same orbital plane as a single system, the coverage area curves are obtained for both the nadir pointing and the rolled configurations.

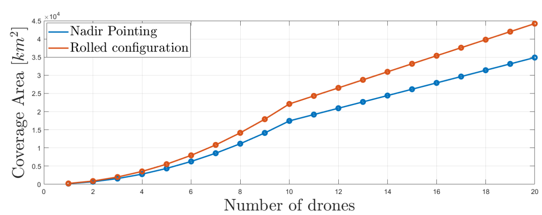

Figure 13: Coverage Area Curves

In Fig. 13 it is evident that for operations requiring more than ten drones the coverage area curve is no more quadratic, so the benefits coming from the augmentation of the fleet are less evident. It is important to highlight that the maximum area covered by twenty drones nadir pointing can be covered by sixteen drones assuming the limit roll angle after a slew, which would be a big benefit in terms of costs and complexity. For the nadir pointing configuration, a single drone can cover 174.41 km^2, while using a twenty-drones formation up to 34877.14 km^2 can be covered, with a total swath width of $SW_{sys} = 264.13\ km$. With the rolled configuration instead, the maximum coverable area spans

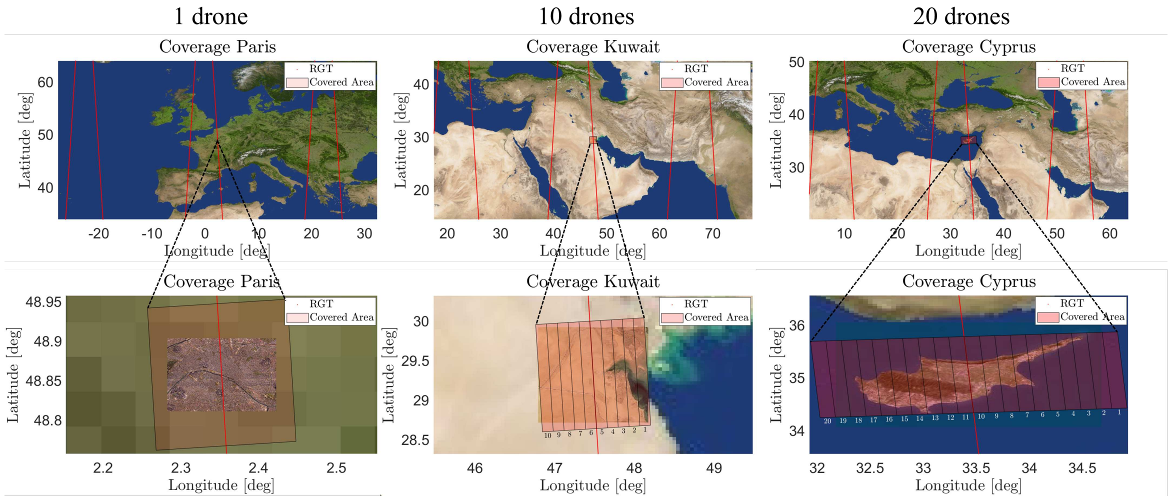

Figure 12: Repeating ground tracks and details with three target examples with different surface area

from 221.12 km^2 with one drone up to 44217.71 km^2 with 20 drones. These two curves represent just the upper and lower bounds of the area covered by a certain number of drones, but it is clear that any intermediate requirement in terms of coverage can be satisfied, after rigorous assessments and trade offs between coverage, spatial resolution, cost and complexity, to guarantee the maximum flexibility. For the sake of clarity, in Fig. 12 three examples of the adoption of this scalable architecture are presented.

The scalable architecture solution is not always guaranteed, though: some areas around the world do not allow multiple drone passages due to the location of the ground stations encountered within one hour from the data acquisition. The result is that for some targets either a drone limit or a continuity limit exist, leading to limited surface areas or discontinuous ones.

In the example previously shown (Fig. 12), 20 drones where needed to cover the whole surface of Cyprus. However possible under a mission analysis point of view, due to downlink time and ground station availability only 19 out of 20 stripes would be transmitted to ground within the hour after acquisition, generating the incomplete image portrayed in Fig. 14.

The remaining set of images can generally be available on ground no longer than 2 hours after the initial acquisition.

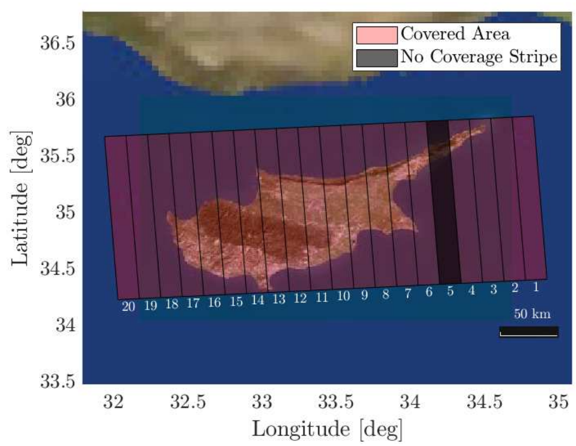

Figure 14: Coverage stripes over Cyprus

5.2 *Revisit Time Performances*

From Section 3.1 and Section 3.7, with multiple orbital planes the orbital parameters for the $i-th$ drone at the starting epoch are set as follows:

$$\begin{cases} a_i = 6640.75\ km \\ e_i = 0 \\ i_i = 90° \\ \Omega_i = \lambda_T + \Delta\Omega_i + 360° \left(\frac{Date_{j2000} - Spring_{j2000}}{365.25\ days}\right) \\ \omega_i \in [0, 360°] \\ \theta_{0,i} = -\sqrt{\frac{\mu}{a^3}}\ ToF_i \end{cases} \quad (25)$$

The peculiarity of dealing with polar and circular orbits is that the Keplerian parameters are easily linked with the mission requirements.
It is important to highlight that some requested imaging times can lead to collisions between two drones at the poles. Considering the $i-th$ and the $j-th$ drones belonging to different orbital planes, the following conditions hold:

$$\begin{cases} (UTC_{T-NP})_i - (UTC_{T-NP})_j \neq k\, T_{orb} \\ (UTC_{T-NP})_i - (UTC_{T-SP})_j \neq k\, T_{orb} \end{cases} \tag{26}$$

where $k \in N$, UTC_{T-NP} is the UTC time at which one drone passes above the North Pole arriving from the target, and UTC_{T-SP} is analogous for the South Pole. Providing a practical example, if the customer asks for a drone to take images at 9:00 UTC and another one to take images at 12:00 UTC , if their passage above the target is in the same direction (i.e. both Northward or Southward), the two drones involved are going to collide, as the time to reach the pole after the imaging is the same and the two requested times differ by 3 h, which is close to the double of the orbital period $T_{orb} = 1.496\ h$.

Adopting a proper margin, it is necessary to delay one of the two requested imaging times by few minutes, so, in the example depicted in Fig. 15, it is sufficient to delay one imaging mode from 9:00 to few minutes later to give a margin and avoid the risk of collision between the 5^{th} and the 7^{th} drones.

5.3 Orbit Maintenance

To validate the effectiveness of the proposed control strategy under realistic operational conditions, an orbital propagation was carried out over a 120-day period.

The simulation assumes the worst-case scenario for station-keeping, characterized by the lowest ballistic coefficient and peak solar activity, resulting in the highest expected atmospheric density[20]. Atmospheric drag was modeled using the *NRLMSISE-00* empirical atmosphere, allowing for time and location-dependent density variations. The spacecraft was initialized at a nominal circular orbit with an altitude of 262.75 km. The analysis aims to evaluate the evolution of the key orbital parameters, assess the control authority of the DAG algorithm in maintaining the desired orbit, and quantify the thrusting effort required to satisfy both altitude and phasing constraints throughout the mission timeline. These constraints define the orbital environment required to fulfill the imaging performance and target coverage requirements. The simulation is therefore intended to demonstrate the system's ability to preserve such parameters over time, validating the proposed control strategy under representative operational scenarios.

The results confirm the ability of the proposed guidance strategy to maintain the satellite orbit within tight constraints over the entire propagation period. As shown in Fig. 16, the semi-major axis remains consistently bounded around the nominal value, showing a periodic behavior due to the on/off thrusting pattern. As shown in Fig. 17, the correction events exhibit high frequency and temporal regularity, characteristic of the on/off thrusting pattern.

The phasing error, Fig. 18, also remains confined within strict bounds, ensuring repeatability of the ground track and precise alignment with the target. The slight drift in the phasing error is due to the assumption of constant thrust, while air density varies slightly over time. Despite this, the error remains well within bounds. A dynamic thrust modulation could easily compensate for this effect, which was not considered in this analysis.

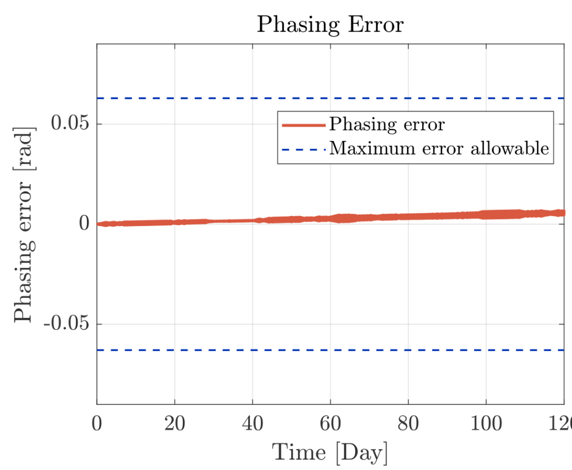

Figure 18: Phasing error over 120 days.

While the control law prioritizes the semi-major axis and phasing, other orbital elements are continuously monitored. The eccentricity is passively stabilized, with small excursions effectively damped by the control logic whenever the value approaches critical thresholds. The inclination shows a slow secular drift, confirming that out-of-plane perturbations are negligible over the considered horizon and no corrective maneuvers are required under nominal conditions.

The evolution of the thrust direction over time, presented in Fig. 19, highlights the alignment of the actuation vector with the computed velocity vector in the RCN frame. This configuration avoids the need for attitude reorientation between thrusting phases, thereby simplifying on-board operations and reducing pointing-related disturbances. The thrust is applied intermittently, over short durations once per orbit, and always at fixed magnitude along the DAG-computed direction. This approach ensures efficient fuel usage while preserving the responsiveness required to counteract drag-induced perturbations with high temporal resolution.

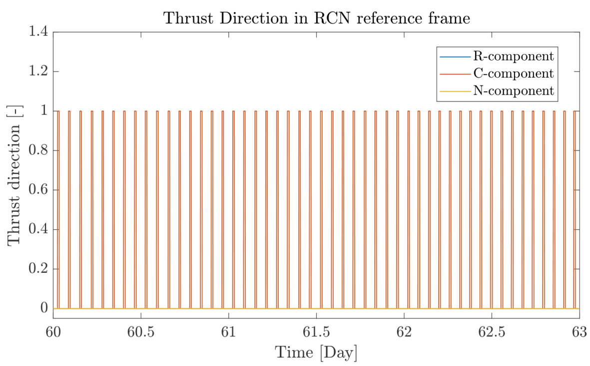

Figure 19: Thrust direction in the RCN reference frame over one day.

Mission lifetime with the proposed station-keeping law was estimated through a straightforward simulation under conservative assumptions, in line with previous analyses. The analysis explicitly tracks three limiting quantities: the total cumulative thrusting time, number of maneuver cycles, and propellant consumption. In this setting, the dominant constraint is the maximum number of ignition cycles supported by the Hall-Effect Electric Thruster (HEET), as summarized in Table 3a. The run returns 9500 maneuvers and about 2186 hours of cumulative thrusting, for a nominal Xenon usage of 3.4 kg. With the total propellant on board, this corresponds to a worst-case lifetime of roughly 594 days; see Table 3b.

A propellant margin is explicitly retained to accommodate off-nominal needs (e.g., occasional out-of-plane trims, re-tasking/phasing adjustments, density surges, and end-of-life contingencies). The required margin is not fixed at this stage and will be traded as the design matures, in concert with refined duty cycles for thrusting and imaging. The current high margin can be adjusted later without affecting nominal performance.

Table 3: Lifetime analysis summary.

(a) Lifetime limiting parameters.

Total thrusting time [h]	2186
Total maneuvers	9500
Propellant used [kg]	3.4

(b) Summary of station-keeping results.

BC [kg/m^2]	230.62
Maneuvers per day	16
Thrusting time [min/man]	13.8
Lifetime [days]	594

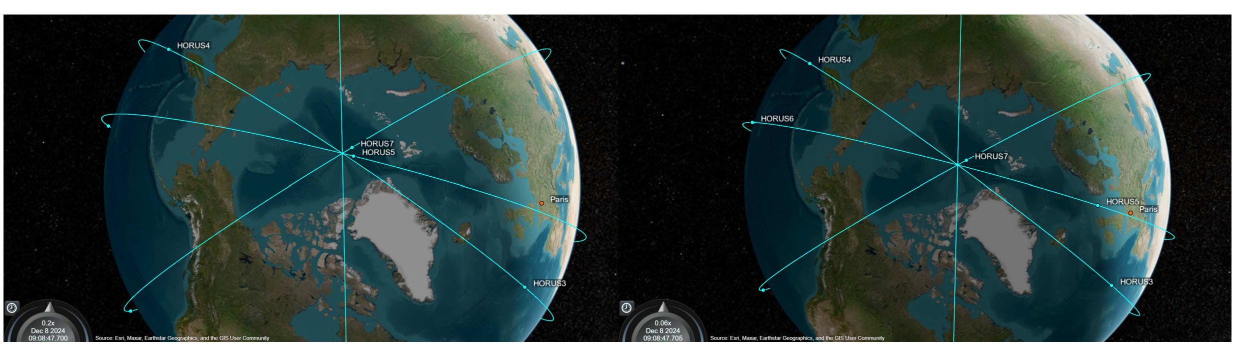

Figure 15: Collision (left) vs collision avoided by renegotiation (right)

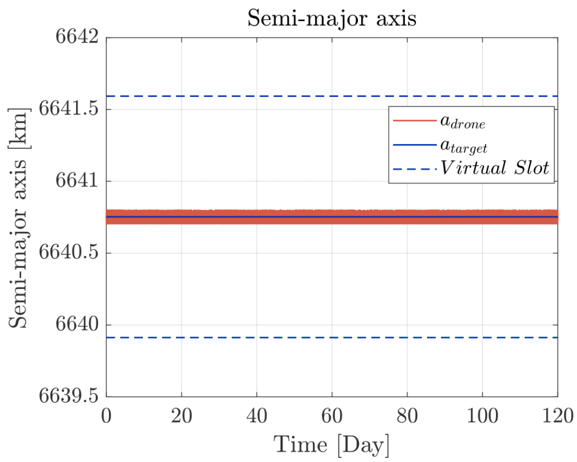

Figure 16: Semi-major axis evolution, 120 days

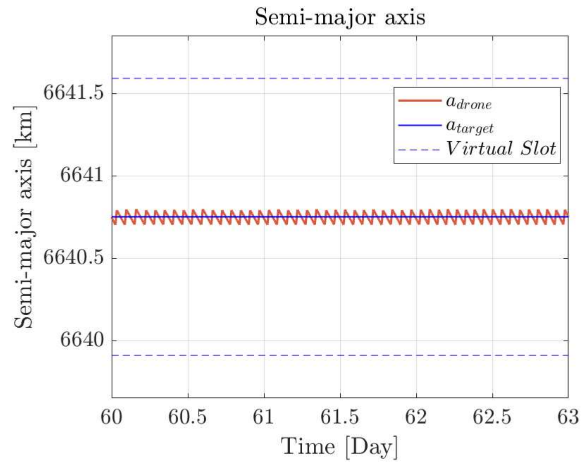

Figure 17: Zoom from day 60 to day 63

6 Conclusions

Design choices and simulations proved that a mission such as HORUS can be achieved with the current technological and scientific knowledge, if carefully adjusted to the high-risk yet high-potential VLEO domain. The iterative process followed along the way, conducted under the ECSS standards, constitutes a closed loop design that took into account all the mission subsystems.

Starting from the mission requirements, the MA proposed solutions have been outlined along with some ingenious drafts regarding the beginning and end of life of the mission; the payload and telecommunications specifics have been presented, pointing out how some design choices and numerical analyses could help reaching the significant coverage performances required by the mission goals and achieved in the simulation environments. The next section evolves around the GNC strategies elaborated in strong synergy with the physical and environmental characteristics of the atmospheric layer of interest. The best-suited GNC strategy - the Directional Adaptive Guidance - has been presented, motivated and applied specifically to the mission here profiled, including references to the propulsion system choices and their impact.

The mission requirements are satisfied, by means of numerical simulations, not without criticalities and limitations; nonetheless, the fundamental objective of designing operational MA and GNC features in a VLEO-intended mission is attained, demonstrating that this harsh environment is no longer a barrier to break, but rather a new domain to explore.

References

[1] Chan Yuk Chi, Indraji Ushantha Wanigaratne, and David Dubinsky. “How low can you go: Advocating very low Earth orbit as the next frontier for satellite operations”. In: *8th European Conference on Space Debris, Darmstadt, Germany.* 2021.

[2] “The GOCE Gravity Mission: ESA’s First Core Earth Explorer”. In: *Proceedings of the 3rd International GOCE User Workshop*. Frascati, Italy: ESA Special Publication SP-627, 2007, pp. 1–8. ISBN: 92-9092-938-3.

[3] “Operating GOCE, the European Space Agency’s Low-flying Gravity Mission”. In: *SpaceOps 2010 Conference: Delivering on the Dream.* American Institute of Aeronautics and Astronautics. 2010. DOI: 10.2514/6.2010-2125.

[4] Isil Sakraker et al. “QARMAN: An Atmospheric Entry Experiment on CubeSat Platform”. In: *Envisat Symposium SP-636*. European Space Agency. 2015. URL: https://www.researchgate.net/publication/277891078_QARMAN_AN_ATMOSPHERIC_ENTRY_EXPERIMENT_ON_CUBESAT_PLATFORM.

[5] EO Portal. *Planet Satellite Missions-SuperDove.* URL: https://www.eoportal.org/satellite-missions/planet.

[6] S. Huang, C. Colombo, and F. Bernelli-Zazzera. "Multi-criteria design of continuous global coverage Walker and Street-of-Coverage constellations through property assessment". In: *Acta Astronautica* 188 (2021), pp. 151–170. ISSN: 0094-5765. DOI: 10.1016/j.actaastro.2021.07.002.

[7] Andrea Garulli et al. "Autonomous Low-Earth-Orbit Station-Keeping with Electric Propulsion". In: *Journal of Guidance, Control, and Dynamics* 34.6 (2011), pp. 1683–1693. ISSN: 0731-5090. DOI: 10.2514/1.52985.

[8] Enrico Belloni et al. "Relative and absolute on-board optimal formation acquisition and keeping for scientific activities in high-drag low-orbit environment". In: *Advances in Space Research* 73.11 (June 2024), pp. 5595–5613. ISSN: 0273-1177. DOI: 10.1016/j.asr.2023.07.051.

[9] Rob Falck et al. "Comparison of Low-Thrust Control Laws for Applications in Planetocentric Space". In: *Conference Paper*. July 2014. DOI: 10.2514/6.2014-3714.

[10] A. Ruggiero et al. "Low-Thrust Maneuvers for the Efficient Correction of Orbital Elements". In: *IEPC-2011-102*. Presented at the 32nd International Electric Propulsion Conference, Wiesbaden, Germany, September 11-15, 2011. Sept. 2011.

[11] ESA. *New Space Debris Mitigation Policy and Requirements in effect*. 2024. URL: https://esoc.esa.int/new-space-debris-mitigation-policy-and-requirements-effect.

[12] NASA. *Deorbit Systems*. 2024. URL: https://www.nasa.gov/smallsat-institute/sst-soa/deorbit-systems/.

[13] Satlantis. *iSIM 90 - Main Features*. URL: https://satsearch.co/products/satlantis-isim-90.

[14] ESA. *Estrack ground station network*. 2025. URL: https://www.esa.int/Enabling_Support/Operations/ESA_Ground_Stations/Estrack_ESA_s_global_ground_station_network.

[15] LeafSpace. *LeafSpace ground station network*. 2025. URL: https://leaf.space/gs-network-and-deployment-plan/.

[16] Swedish Space Corporation. *SSC ground station network*. 2025. URL: https://sscspace.com/services/satellite-ground-stations/.

[17] Bruce Bowman and Frank Marcos. "A New Empirical Thermospheric Density Model JB2006 Using New Solar Indices". In: 1 (Aug. 2006). DOI: 10.2514/6.2006-6166.

[18] Meysam Mahooti. *NRLMSISE-00 Atmosphere Model*. https://www.mathworks.com/matlabcentral/fileexchange/56253-nrlmsise-00-atmosphere-model. 2024.

[19] A. Garulli et al. "Autonomous Low-Earth-Orbit Station-Keeping with Electric Propulsion". In: *Journal of Guidance, Control, and Dynamics* 34.6 (2011), pp. 1593–1600. DOI: 10.2514/1.52985.

[20] Kh.I. Khalil and Susan Samwel. "Effect of Air Drag Force on Low Earth Orbit Satellites During Maximum and Minimum Solar Activity". In: *Space Research Journal* 9 (Mar. 2016), pp. 1–9. DOI: 10.3923/srj.2016.1.9.